

Research article

Exploring the potential of *in-situ* foam 3D printing: Effects of printing parameters and the development of functionally graded foams

Viktória Kunsági^{ID}, Péter Széplaki^{ID}, Márton Tomin^{*ID}

Department of Polymer Engineering, Faculty of Mechanical Engineering, Budapest University of Technology and Economics, Műegyetem rkp. 3., H-1111 Budapest, Hungary

Received 25 March 20258; accepted in revised form 22 April 2025

Abstract. In this study, we investigated the influence of processing parameters on the cellular structure and density of specimens fabricated using *in-situ* foam 3D printing. First, we conducted a comprehensive analysis to examine how the combined effects of printing temperature and speed influence the four key stages of the foaming process: gas dissolution, cell nucleation, cell growth, and stabilization. By evaluating the structural characteristics of the printed foams, we identified the dominant mechanisms governing each stage. Next, we explored the effect of nozzle diameter, an aspect previously unexamined in the literature. We found that smaller nozzle diameters promote higher cell density due to enhanced pressure drop and shear-induced nucleation, resulting in a 36.8% reduction in density and a 60.3% increase in cell density when using a 0.4 mm nozzle instead of 0.8 mm (at 240 °C, 60 mm/sec). Finally, we fabricated functionally graded four-layer structures by adjusting the printing temperature for each layer to control porosity distribution. To evaluate the mechanical performance of these graded structures, we performed three-point bending and drop-weight impact tests, allowing us to assess how layer order influences mechanical properties. Our results showed that proper layer sequencing can increase flexural strength by up to 69.4% and improve perforation energy by more than 94.8% compared to homogeneous structures.

Keywords: 3D printing, foam, additive manufacturing, fused filament fabrication, functionally graded design

1. Introduction

3D printing is becoming an increasingly widespread manufacturing technology and is growing rapidly due to its many advantages over traditional manufacturing processes [1]. The technology allows for the rapid production of complex geometries and customized parts, reduces manufacturing waste, and shortens prototyping and final product production times [2]. These benefits contribute to the widespread use of 3D printing for prototyping and final products in many industries, including automotive, aerospace, and medical [1, 2]. Based on a report issued by Strategic Market Research (Report ID: 80536350), the global 3D printing industry was worth

\$16.94 billion in 2022 and is predicted to grow to \$77.83 billion by 2030.

FDM/FFF (Fused Deposition Modeling/Fused Filament Fabrication) technology is one of the most widely used 3D printing processes, mainly due to its simplicity, cost-effectiveness, and wide availability of materials [3, 4]. FDM printers are among the filament-forming additive manufacturing processes, where a melted polymer is extruded through a heated nozzle to create the desired geometry layer by layer [5, 6]. This method has become popular not only in the industrial sector, but also among home hobby printers, and the number of printers sold is increasing every year [7]. According to the industry forecast of

*Corresponding author, e-mail: tominm@pt.bme.hu
© BME-PT

Grand View Research (Report ID: GVR-4-68040-270-8), the market for FDM printers is expected to grow at a compound annual growth rate of 21.8% between 2024 and 2030, reaching a market value of \$3 billion by the end of the decade.

However, the more widespread use of this technology for technical purposes is limited by the anisotropy of the printed specimens and the weak adhesion between the deposited layers, which results in weaker mechanical properties [8]. This problem can be solved by the use of *in-situ* foamable filaments containing chemical (CBA) or physical (PBA) blowing agents or thermally expandable microspheres (TEM). During printing, the elevated temperature causes the foaming agents to decompose, releasing gas. As the material exits the nozzle, the sudden pressure drop triggers expansion, which can help eliminate interlayer gaps and weak adhesion. This improvement in layer bonding can lead to enhanced mechanical performance of the printed parts [9]. Additionally, the use of these filaments enables the controlled adjustment of printing parameters during manufacturing, allowing for the creation of functionally graded sandwich structures with tailored porosity [9–13]. Such graded structures can also be produced using specialized techniques, such as static mixer nozzles with dual flow paths, where foaming and non-foaming filaments are combined to achieve programmable density profiles [14]. These density-graded structures, featuring variations in cellular properties across the thickness, exhibit superior mechanical performance compared to homogeneous structures of the same weight [15, 16]. Despite the increasing research interest in process-controlled foaming, the effect of nozzle diameter – an essential parameter influencing pressure drop, shear rate, and residence time – has remained largely unexplored in this context.

In recent years, increasing efforts have been made to better understand the mechanisms of *in-situ* foam formation during 3D printing, particularly with the aim of optimizing cellular structure and mechanical performance. A research group at the University of Massachusetts Lowell has published multiple studies on the development of polylactide acid (PLA) filaments containing TEM particles. By incorporating triethyl citrate as a plasticizer, they successfully reduced the processing temperature, thereby preventing undesired pre-foaming during filament production [9, 17]. Their investigations also explored the impact of the PLA matrix material's melt flow index

on foaming behavior, as well as the effects of varying flow rates and printing temperature [17]. They concluded that residence time and temperature play a critical role in the expansion of microspheres, significantly influencing the homogeneity of the resulting cell structure [18]. Utilizing these insights, they created multilayered structures in which porosity was controlled through printing parameter adjustments [19]. Similarly, Nieduzak *et al.* [20] developed foaming filaments using TEM particles in an rHDPE/PP blend and found that the use of *in-situ* foam 3D printing helped reduce the warping of printed specimens. However, in these studies, the foaming process was simplified by the presence of TEM particles, which facilitated cell nucleation and controlled expansion. While this approach is effective, TEM shells are non-biodegradable, and the material itself is relatively expensive, limiting its applicability in certain fields.

Other foaming strategies, such as CO₂-based physical foaming, rely on a more complex interaction of gas dissolution, nucleation, and growth. In this field, Peng *et al.* [21] demonstrated that *in-situ* foaming of PLA/chitin nanocrystal scaffolds during 3D printing allows for tunable porosity and improved interlayer adhesion by adjusting nanofiller content and printing speed, while Zhang *et al.* [22] investigated the effect of printing temperature and speed on the resulting porosity by using supercritical CO₂-saturated thermoplastic polyurethane filaments. However, as demonstrated by Li *et al.* [11] on CO₂-saturated polyetherimide and PLA filaments, gas saturation in the filament prior to printing requires significant time (24–48 h), and maintaining the dissolved gas in the system until printing is challenging, which suggests that CBAs could offer a more practical alternative [10].

Damanpack *et al.* [23] investigated the effects of printing temperature and flow rate on porosity and mechanical properties using a commercially available PLA filament with an endothermic CBA. They examined how changes in temperature influenced density and mechanical performance, while they adjusted the flow rate accordingly to ensure consistent interlayer adhesion across all conditions. The effect of printing parameters such as temperature and speed was also analyzed by Ozdemir and Doubrovski [24], who investigated how these parameters influence the expansion behavior of a commercially available *in-situ* foamable filament (LW-PLA by Colorfabb).

However, their primary focus was on changes in optical properties (e.g., color and translucency), while neither the resulting cellular structure nor the mechanical properties of the printed foams were evaluated. To improve CBA foaming efficiency, Choi *et al.* [25] enhanced the melt strength of PLA by using an epoxy-based chain extender, which improved foamability by promoting more stable cell nucleation and growth, resulting in a homogeneous cell structure. As their aim was material development, they kept the printing parameters fixed throughout the experiments.

Although these previous studies have revealed valuable results on the process of *in-situ* foam 3D printing, several important underlying mechanisms remain unexplored. Most of the research investigates the effect of a specific processing parameter separately, despite the fact that these parameters have a combined influence on the different stages of the foaming process (gas dissolution, cell nucleation, cell growth, and stabilization). In addition, it is important to highlight that the current studies all used one type of nozzle, so the effect of nozzle geometry has not been explored. Since nozzle diameter affects shear rate, pressure, and residence time during printing, it is likely to influence cell nucleation and growth. A deeper understanding of this relationship may contribute to better control of the porosity distribution and mechanical performance of functionally graded foams.

In this study, our main goal was to understand more deeply how printing parameters, such as temperature

and speed, influence the foaming behavior of PLA filaments containing a chemical blowing agent. While the effects of temperature and speed have already been examined in previous works, the impact of nozzle diameter has remained unexplored, despite its relevance to shear rate, residence time, and pressure drop. By including nozzle diameter as a variable, our work addresses this knowledge gap and contributes to a deeper understanding of its role in cell nucleation and foam morphology. To further explore the potential of process-controlled foaming, we conducted a case study in which four-layer graded structures were fabricated by adjusting printing parameters. The influence of layer order on mechanical performance was also evaluated.

2. Experimental

The aim of our research was to investigate the expansion of *in-situ* foaming filaments during 3D printing and the resulting cell structure. In the first stage, the effects of printing temperature and speed were analyzed using different parameter combinations. In the second phase, the influence of the nozzle diameter on the foaming mechanism at different printing temperatures was investigated. Finally, we created four-layer, functionally graded foam structures by applying different printing temperatures for each layer. We evaluated the effect of layer-order modification on the mechanical properties by performing 3-point bending and falling weight impact tests. The schematic representation of the experimental process is shown in Figure 1.

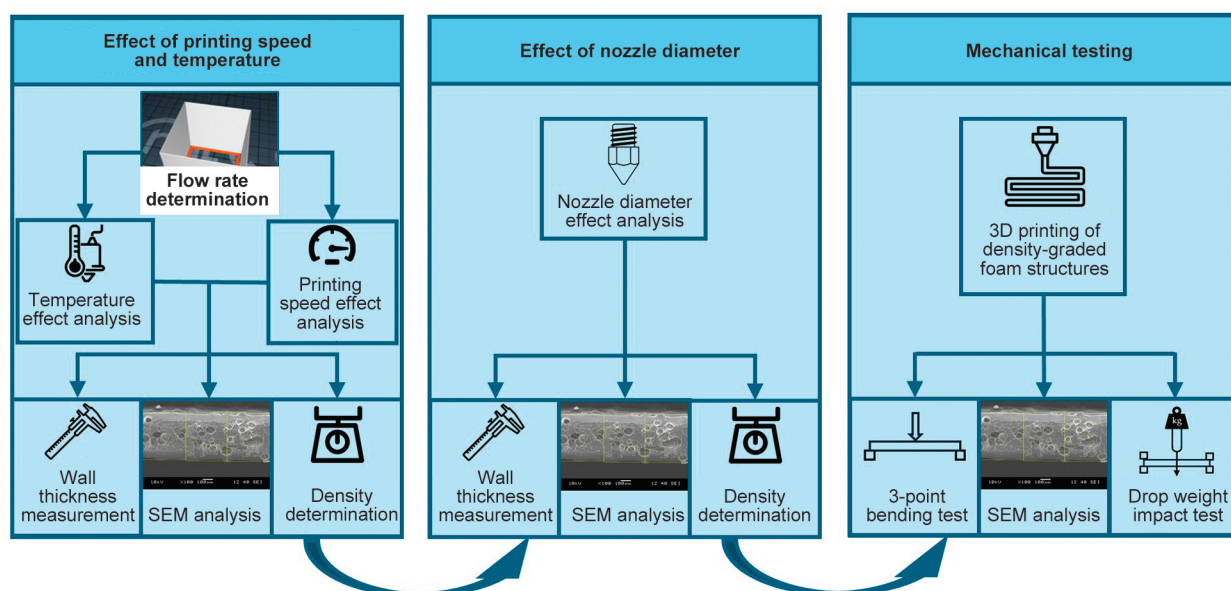


Figure 1. Schematic representation of the experimental process.

2.1. PLA filament

In order to evaluate the effect of printing parameters, a commercially available material, namely LW-PLA by Colorfabb (Belfeld, Netherlands), was used as an *in-situ* foamable filament for the tests. The material has a glass transition temperature range of 55–60 °C, a melting temperature range of 150–160 °C, and a melt flow index of 6 g/10 min (210 °C/2.16 kg). The activation temperature of the foaming agent is 230 °C according to the manufacturer's datasheet, and the recommended print settings are 195–260 °C nozzle temperature, 40–100 mm/s print speed and 50–60 °C bed temperature. The material is expanding during the 3D-printing process due to the presence of the endothermic blowing agent in the system [23].

2.2. 3D printing

All specimens were fabricated using a Craftbot Plus (CraftUnique Ltd., Budapest, Hungary) FDM printer. The slicing software used was CraftWare, the proprietary slicer developed by CraftUnique for Craftbot printers, ensuring optimized compatibility with the machine. We conducted three experimental phases to systematically investigate the effects of printing parameters on the *in-situ* foaming process.

2.2.1. Effect of printing temperature and speed

In the first phase, we focused on analyzing the influence of printing temperature and speed on foaming behavior. For that purpose, hollow cubes (25×25×25 mm) with a nominal wall thickness of 0.4 mm were printed. A 2 mm outer brim was added to improve bed adhesion. Printing was performed using a 0.4 mm MK8 steel nozzle, with a layer height of 0.2 mm and an extrusion width of 0.4 mm. The cooling fan was set to 100%, and the bed temperature remained constant at 60 °C. The extrusion multiplier was set to 1 (100% flow rate) for all specimens to ensure a consistent material input and nominal layer geometry in the absence of foaming, allowing a clear comparison of the effects of speed and temperature. The effect of printing temperature was examined over a range of 190–250 °C, while printing speed was varied between 20 and 60 mm/s. Both parameters were adjusted in increments of 10 °C and 10 mm/s, respectively. From the printed specimens we performed density measurement, SEM analyses and determined the rate of expansion using the methods described in Section 2.3–2.4.

2.2.2. Effect of nozzle diameter

In the second phase of the research, we investigated the influence of nozzle diameter while keeping the printing speed fixed at 60 mm/s. To analyze its effect on foaming behavior, hollow cubes with dimensions of 25×25×25 mm and a single-layer wall thickness were printed using three different MK8 steel nozzles with diameters of 0.4, 0.6, and 0.8 mm. The 0.4 mm nozzle, already used in the first phase of the study, served as a reference for comparison. For the larger nozzle diameters, the layer height and extrusion width were adjusted to maintain consistent proportions. For the 0.6 mm nozzle, the layer height was set to 0.3 mm, with an extrusion width of 0.6 mm, while for the 0.8 mm nozzle, the layer height was 0.4 mm, and the extrusion width was 0.8 mm.

To examine the relationship between nozzle size and foaming behavior, printing was conducted at temperatures ranging from 220 to 250 °C in 10 °C increments. Since the nozzle diameter directly influences shear rate, pressure, and residence time during printing, it is expected to have a significant impact on cell nucleation and growth dynamics. By systematically varying the nozzle size while keeping other parameters constant, we aimed to explore how these factors affect the cellular characteristics of the printed structures.

2.2.3. Residence time and shear rate calculation

Estimation of wall shear rate

To evaluate the shear conditions experienced by the material during printing, a theoretical approach was employed to estimate the wall shear rate based on nozzle geometry and printing speed. The purpose of the analysis was to understand how variations in nozzle diameter influence the shear rate and, consequently, the apparent viscosity of the material. The wall shear rate $\dot{\gamma}_w$ [1/s] was estimated using the following expression, which assumes axisymmetric flow (Equation (1)) [26]:

$$\dot{\gamma}_w = \frac{4Q}{\pi R^3} \quad (1)$$

where Q [mm³/s] is the volumetric flow rate, and R [mm] is the internal radius of the nozzle. The volumetric flow rate Q can be substituted by the product of the cross-sectional area of the nozzle and the average flow velocity (Equation (2)):

$$Q = A \cdot v_{\text{print}} = \frac{D^2 \pi}{4} \cdot v_{\text{print}} \quad (2)$$

where v_{print} [mm/s] denotes the printing speed, and D [mm] is the internal diameter of the nozzle. Recognizing that $R = D/2$ we obtain Equation (3):

$$\dot{\gamma}_w = \frac{4 \left(\frac{D^2 \pi}{4} \cdot v_{\text{print}} \right)}{\pi \left(\frac{D}{2} \right)^3} \quad (3)$$

This expression provides an estimate of the apparent wall shear rate under steady-state flow conditions. The calculation was repeated for a range of nozzle diameters to quantify the sensitivity of shear rate to geometric changes. This approach allows for a comparative analysis of the effect of nozzle design on shear-driven flow behavior, which is especially relevant in applications such as extrusion or material deposition.

Residence time estimation

The melting of the filament is a fundamental process in FDM-based 3D printing technology. This occurs inside the nozzle, where different printing speeds and nozzle diameters result in different residence times. As a result, the foaming agent present in the filament is subjected to varying durations of thermal exposure, which influences its activation and the degree of foaming.

To calculate the residence time, we considered the internal geometry of the nozzle to estimate how quickly the material flows through it at given printing

speeds. We formulated the following expression to estimate the residence time of the material inside the nozzle, taking into account the relevant geometric and process parameters (Equation (4)):

$$t_r = \frac{h_{\text{nozzle}}}{\frac{v_{\text{print}} \cdot h_{\text{layer}} \cdot D}{A_{\text{filament}}}} \quad (4)$$

where h_{nozzle} [mm] represents the height of the molten filament inside the (vertical) nozzle, v_{print} [mm/s] denotes the printing speed, h_{layer} [mm] is the layer height, D is the nozzle diameter [mm] and A_{filament} [mm²] corresponds to the cross-sectional area of the filament, given in square millimeters.

2.2.4. Fabrication of density-graded multilayer foam structures

As the final part of this research, we conducted a case study to demonstrate the potential of *in-situ* foam printing for producing density-graded multilayer foam structures. To achieve this, we fabricated four-layer structures with layer-by-layer variations in printing temperature, creating a controlled porosity gradient along the thickness. The specific temperature profiles used for these configurations are presented in Figure 2.

To establish a reference, one set of specimens was printed at a uniform nozzle temperature of 230 °C, resulting in a homogeneous structure. The second configuration followed a sandwich-like approach, with the first and final 1 mm layers printed at 210 °C, while the interior 2 mm section was printed at 250 °C,

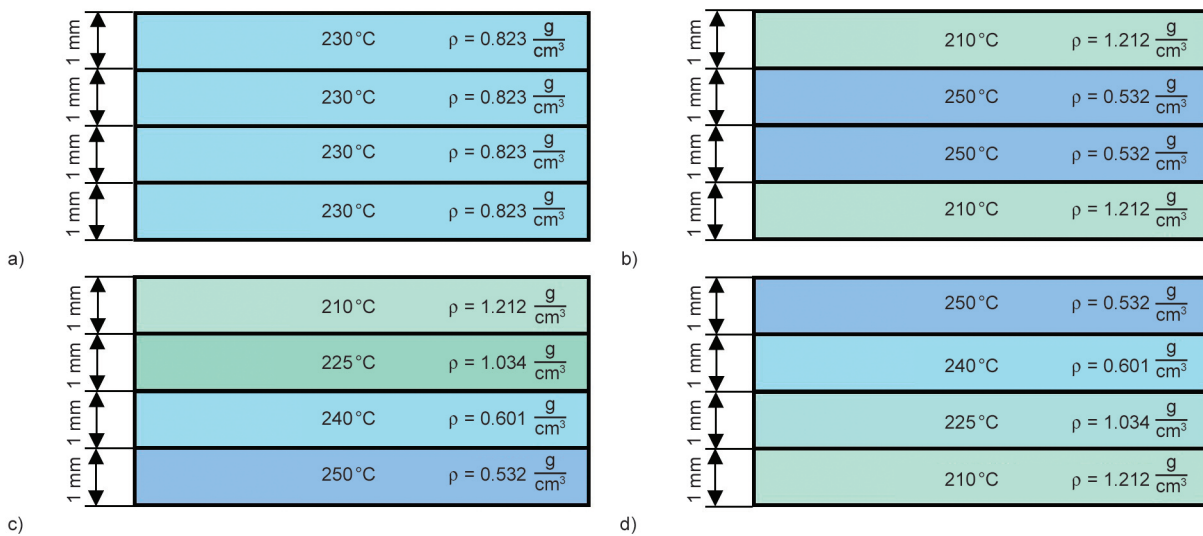


Figure 2. The temperature profiles for the configurations used for the printing of the multilayer structures and resulted density values for the configurations a) printed with 230–230–230–230 °C, b) with 210–250–250–210 °C, c) with 250–240–225–210 °C and d) with 210–225–240–250 °C.

creating a rigid shell with a porous core. The third configuration introduced a gradual temperature variation, with sequential layers printed at 250, 240, 225, and 210 °C from bottom to top. The fourth configuration mirrored this setup in reverse, with the highest temperature layer at the top and the lowest at the bottom. The nozzle diameter for all cases was 0.4 mm, while the printing speed was kept constant at 60 mm/s throughout. The bed temperature was maintained at 60 °C, and the layer height was set to 0.2 mm. The size of the test specimens was 80×10×4 mm (ISO/R 178) for the bending, while 80×80×4 mm for the falling weight impact tests.

To ensure consistency in sample dimensions despite the variable expansion caused by foaming at different temperatures, the extrusion multiplier was used for each layer to adjust flow rate (Equation (5)) [27, 28]:

$$\text{Extrusion multiplier} = \frac{w_0}{w_i} \quad [-] \quad (5)$$

where w_0 [mm] is the average wall thickness of the unfoamed specimen (printed at 190 °C), while w_i [mm] is average wall thickness of the foamed specimen (printed at a given temperature), which were determined by measuring the thickness of each of the four sides of the printed hollow cubes with a Mitutoyo CD-15APXR type vernier caliper. This adjustment ensured that the overall sample volume remained consistent across all layer configurations.

Since the slicing software did not support direct modification of process parameters within a single G-code file, manual G-code editing was required to apply layer-specific temperature and extrusion multiplier settings. The nozzle temperature was modified using the M109 SXXX command, where XXX denotes the target temperature (e.g., M109 S210 for 210 °C). The M109 command instructs the printer to wait until the desired temperature is reached before executing any subsequent commands, ensuring that each layer is printed at the correct temperature. To prevent material leakage while waiting for the temperature adjustment, the printhead was moved to the home position along the X-Y axis using G28 X Y before resuming printing. To implement layer-specific flow rate adjustments, we calculated the required extrusion multiplier for each layer using Equation (5). This value was then used to scale the corresponding E -values in the G-code, which define the length of filament extruded. By multiplying the original E -values with the temperature-specific multiplier, we corrected the material

feed rate directly in the G-code. This ensured that, despite the foaming-induced expansion, the overall dimensions and mass of each printed specimen remained consistent. The modified G-code sections were then merged to create a single file for printing the multilayer structure.

The fabricated multilayer structures were then subjected to three-point bending and falling weight impact tests, as described in Sections 2.5 and 2.6, to evaluate the effect of layer-order modification on mechanical properties. By implementing controlled variations in printing temperature, these experiments aimed to assess how porosity gradients influence mechanical performance, providing insight into the structural optimization of functionally graded foams. To ensure comparability between different layer order configurations, the printing temperatures were selected to achieve similar overall density across all specimens. As a result, the variation in specimen mass remained within 10% in all cases. The density values for each layer are denoted in Figure 2.

2.3. Density and expansion measurement

To quantify the degree of foaming, the expansion ratio was evaluated by measuring the wall thickness of the printed cubes. Additionally, the density of the printed specimens was determined (Equation (6)) at room temperature through hydrostatic measurement, using distilled water as the measuring liquid [29]:

$$\rho_{\text{foam}} = \frac{m_a}{m_a - m_l} \cdot \rho_{\text{dw}} \quad (6)$$

where ρ_{foam} [g/cm³] is the density of printed foam structure, m_a [g] is the mass derived from the weight of the specimen in air, m_l [g] is the mass derived from the weight of the specimen measured in water, ρ_{dw} [g/cm³] is the density of the measuring medium (distilled water).

2.4. Scanning electron microscopy (SEM)

The cell structure of the samples produced with different printing settings (temperature, speed, nozzle diameter) was examined using a JEOL JSM 6380LA scanning electron microscope (Jeol Ltd., Tokyo, Japan). Prior to testing, all samples were immersed in liquid nitrogen to generate cryogenic fracture surfaces, after which they were coated with a gold-palladium alloy to ensure adequate conductivity. The SEM samples were prepared by cutting out the side walls of the printed hollow cubes. Images were taken

at 100× and 200× magnification to assess the cell morphology. Additionally, to examine the effect of layer configuration, SEM images were also taken at 20× magnification from density-graded specimens produced for the mechanical testing. Based on the electron microscopic images and the density of the samples, the degree of expansion (Equation (7)) were determined, which were then used to calculate cell density (Equation (8)) and average cell wall thickness (Equation (9)) [30, 31]:

$$\phi = \frac{\rho_{\text{solid}}}{\rho_{\text{foam}}} \quad (7)$$

$$N_C = \left(\frac{n}{A}\right)^{\frac{3}{2}} \quad (8)$$

$$\delta = \left(3\sqrt{\frac{\phi}{\phi-1} - 1}\right) \cdot l \quad (9)$$

where ϕ [–] is the degree of expansion, ρ_{foam} [kg/m³] is the foam density, ρ_{solid} [kg/m³] is the density of the unfoamed material, N_C [pcs/cm³] is the cell density, n [pcs] is the number of cells visible in the SEM image, A [cm²] is the investigated area on the sample, δ [μm] is the cell wall thickness, and l [μm] is the average cell size. The average cell size was determined by using the ImageJ (National Institutes of Health, Bethesda, USA) image processing software. The cell wall thickness (see Equation (9)) was estimated based on Rangappa and Yeh [32] by assuming a homogeneous closed-cell structure, where the cells are approximated as regular cubes. The calculation was based on the average cell size obtained from SEM images and the degree of expansion, which was determined from the density of the foamed and unfoamed material. This simplified geometric model enables comparative analysis of structures produced under similar processing conditions [31].

2.5. 3-point bending test

The printed density-graded 4-layer specimens were subjected to a three-point bending test in accordance with ISO 178, using a Zwick Z250 universal testing machine (Zwick GmbH, Ulm, Germany) equipped with a 1.0 kN capacity load cell. During the tests, a standard support span of 64 mm was applied with a specimen size of 80×10×4 mm. The loading speed was 5 mm/min. The preload was set to 1 N, with a preload speed of 20 mm/min. The laboratory conditions during testing were maintained at 43.7% relative humidity and a temperature of 23.6 °C.

Throughout the experiment, a force-deflection curve was recorded, from which the flexural strength was subsequently calculated using the following equation (Equation (10)) [33]:

$$\sigma_{\text{fs}} = \frac{3FL}{2bh^2} \quad (10)$$

where σ_{fs} [MPa] is the flexural strength, F [N] is the recorded force, L [mm] is the support span, b [mm] is the specimen width, and h [mm] is the specimen height. In the evaluation, we compared the flexural strength corresponding to a deflection equal to 10% of the support span (*i.e.*, the limit bending stress) for each layer configuration.

Subsequently, the flexural modulus of elasticity for each foam structure was determined using the following equation (Equation (11)) [33]:

$$E_f = \frac{1}{4} \cdot \frac{L^3}{bh^3} \cdot \frac{\Delta F}{\Delta f} \quad (11)$$

where E_f [MPa] is the flexural modulus of elasticity, L [mm] is the support span, b [mm] is the specimen width, h [mm] is the specimen height, and $\Delta F/\Delta f$ [N/mm] is the slope of the force-deflection curve between 0.05 and 0.25% relative elongation. All properties were determined by testing five specimens for each configuration.

2.6. Impact testing

In order to evaluate the effect of layer order modification on the dynamic mechanical properties of the density-graded multilayer structures, we performed drop weight impact tests by using a Ceast Fractovis 9350 (Instron, Torino, Italy) impact tester. Specimens with a dimension of 80×80×4 mm were secured with a clamping ring and impacted by a hemispherical striker with a 20 mm diameter. The impact velocity was set to 3.14 m/s, with an impactor weight of 3.036 kg, resulting in an impact energy of 15 J. During the perforation of the samples, the force-time data was recorded by using a piezoelectric sensor with a 4.5 kN capacity. From these measurements, the maximum force, perforation energy (Equation (12)) and ductility (Equation (13)) index were determined using the following equations [34]:

$$E_{\text{perf}} = \frac{E_{\text{total}}}{v_{\text{sample}}} \quad (12)$$

$$DI = \frac{E_{\text{total}} - E_{F_{\text{max}}}}{E_{\text{total}}} \cdot 100 \quad (13)$$

where E_{perf} [J/mm] is the perforation energy, E_{total} [J] is the total energy absorbed by the specimen during the impact, v_{sample} [mm] is specimen thickness, DI [%] is the ductility index, while $E_{F_{\text{max}}}$ [J] is the energy absorbed up to the moment when the maximum force was recorded. All properties were determined by testing ten specimens for each configuration.

3. Results and discussion

3.1. Effect of printing temperature and speed on foam expansion and cell structure

To achieve the desired controlled foam structure and cell structure, the first step was to investigate the effect of printing parameters on the degree of foaming. The foaming process can be basically divided into four steps: first, the dissolution of the evolving gas in the polymer matrix, followed by cell nucleation due to the pressure drop at the exit of the nozzle, then cell growth, and finally cell stabilization by cooling. Printing temperature and speed play a critical role in these steps. Increasing the printing temperature promotes the dissolution of the gas in the polymer matrix, but can negatively affect the cell stabilization stage, as the reduced melt strength and the higher diffusivity of the gas can lead to cell collapse and cell coalescence. Conversely, increasing the printing speed reduces the residence time of the material in the nozzle, which can negatively affect the dissolution of the gas. At the same time, higher shear and faster exit from the nozzle result in higher pressure drop, which may promote cell nucleation and cell growth. In the first phase of the research, we aimed to investigate the combined effect of printing speed and temperature to determine which parameters dominate in the different foaming stages and how their variations influence the final cell structural characteristics.

To better understand the underlying mechanisms, we used a theoretical approach to estimate the wall shear rate and residence time under each printing condition. These results are presented in Figure 3 and are referenced in Sections 3.1 and 3.2.

The effect of nozzle temperature and printing speed was analyzed by thickness measurement and density testing. The results, summarized in Figure 4, show the trends observed across a 7×5 parameter matrix. The results clearly indicate that at 210 °C and below, no foaming occurred regardless of the printing speed. This is likely due to the blowing agent not decomposing at these temperatures, preventing gas release, which is essential for foam formation. As the temperature increased, a significant decrease in density and an increase in wall thickness were observed. This can primarily be attributed to the greater heat transfer to the polymer, which accelerates the decomposition of the blowing agent. Consequently, a larger amount of gas was released and dissolved in the polymer matrix at higher temperatures. However, when analyzing lower printing speeds (e.g., 20 mm/s), it becomes evident that increasing the temperature beyond a certain optimum negatively affects foaming. This can be attributed to the reduced melt strength at elevated temperatures, making cell stabilization more challenging and leading to increased cell collapse and coalescence.

When evaluating the effect of printing speed on density, different trends can be observed depending on the printing temperature. At lower temperatures (at and below 210 °C), where foaming did not initiate, speed had no measurable effect on density values. For temperatures of 220 °C and 230 °C, increasing the speed resulted in a significant increase in density. This can be explained by the fact that at higher speeds, the residence time of the material in the heated

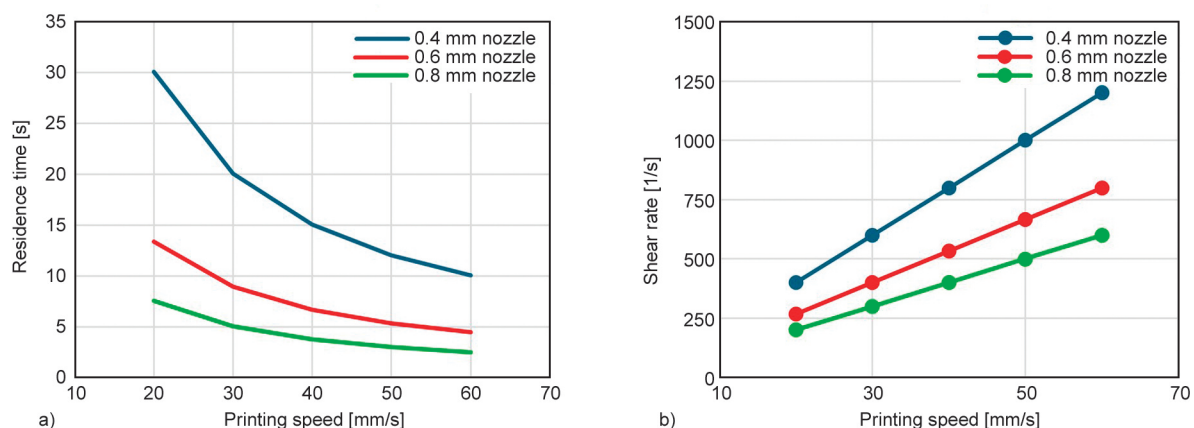


Figure 3. Estimated residence time (a) and wall shear rate (b) as a function of nozzle diameter and printing speed.

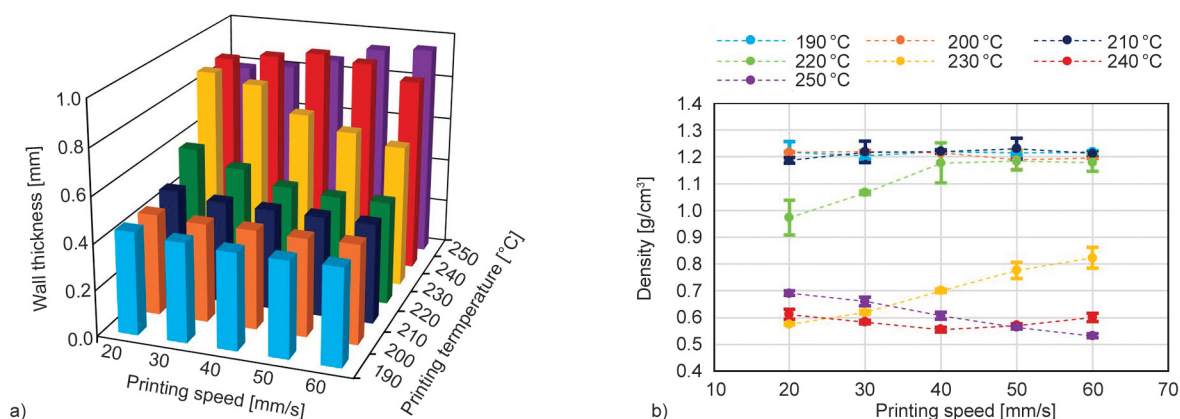


Figure 4. Wall thickness (a) and density (b) of hollow cubes printed with different temperature and speed settings.

nozzle decreases (see Figure 3). Due to the low thermal conductivity of polymers, heat transfer becomes insufficient for complete decomposition of the blowing agent, reducing the extent of foaming.

At 240 °C, the effect of speed on foaming follows a more complex tendency. Initially, increasing speed enhances the degree of foaming, leading to a decrease in density. Suppose the residence time is still sufficient for full decomposition and gas dissolution (as observed at 20, 30, and 40 mm/s). In that case, higher speeds provide an additional benefit by increasing the internal pressure within the nozzle. This leads to a more significant pressure drop at the nozzle exit [35], promoting both cell nucleation and growth. However, beyond a certain threshold (above 40 mm/s at 240 °C), the residence time becomes too short for complete gas dissolution, causing a decline in foaming efficiency.

As the printing temperature increases further, the optimal printing speed for maximum foaming shifts toward higher values. At 250 °C, for instance, the highest speed tested (60 mm/s) resulted in the greatest reduction in density. This suggests that despite the high temperature, the reduced residence time prevented excessive heat exposure, avoiding a severe reduction in melt strength. Additionally, the higher speed contributed to an increased pressure drop at the nozzle exit [35], further facilitating cell nucleation and growth.

To support the findings and analyze the cellular structure, scanning electron microscopy (SEM) images were captured for the cross-sections of printed samples at each parameter setting. Since previous results indicated that foaming was only initiated at 220 °C and above, no images were taken for temperatures below this threshold. The collected images are summarized in Table 1.

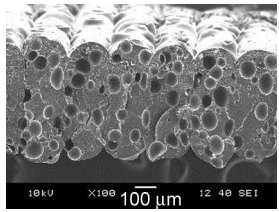
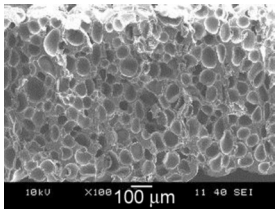
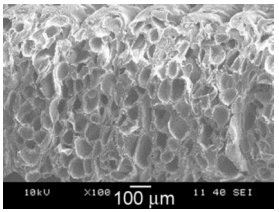
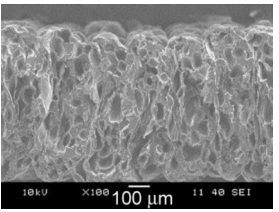
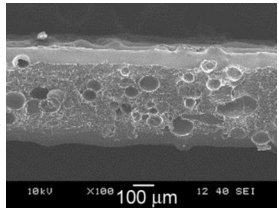
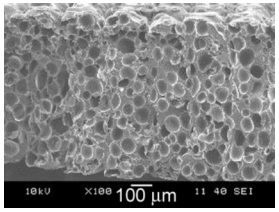
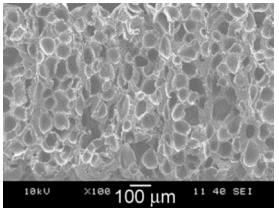
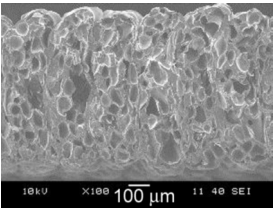
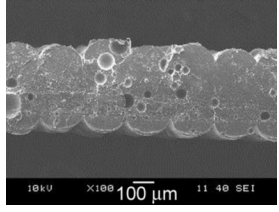
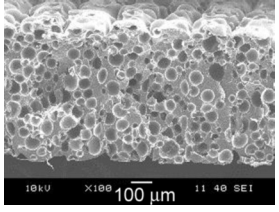
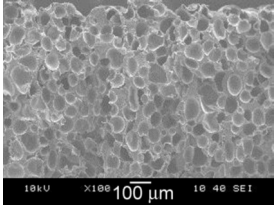
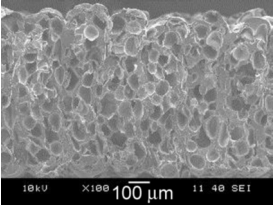
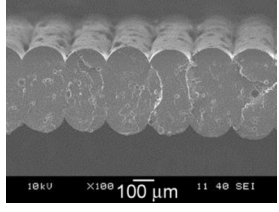
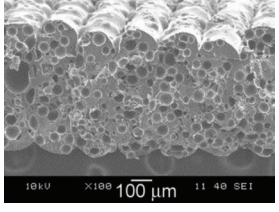
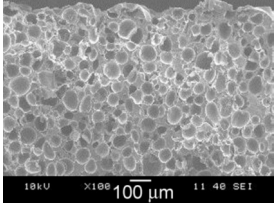
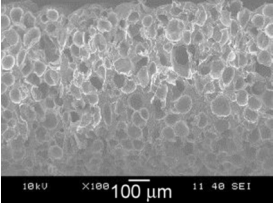
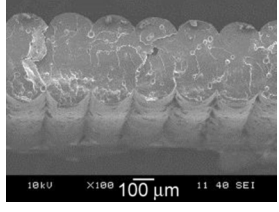
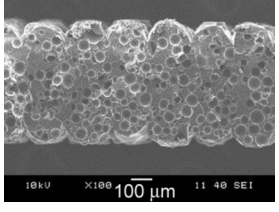
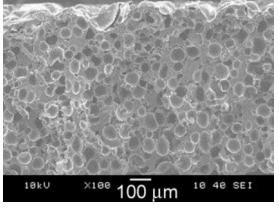
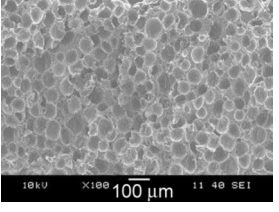
The SEM images reveal that all the printed specimens have a closed-cell structure, allowing further investigation of the influence of printing parameters on cell formation.

At 220 °C, increasing the printing speed drastically reduced the number of visible cells. At a low temperature of 220 °C and high speed of 60 mm/s, no visible pores were detected in the SEM images, which is consistent with the density measurements, indicating that foaming did not occur under these conditions.

In contrast, the cell morphology appeared increasingly irregular at higher temperatures (240 and 250 °C) and low speeds (20 and 30 mm/s). This supports the earlier conclusion that the combination of high temperature and low speed exposed the polymer to excessive thermal loading. The lower melt viscosity at elevated temperatures, combined with the longer residence time, allowed for increased gas diffusion before solidification. Moreover, the faster decomposition rate of the blowing agent at high temperatures, coupled with prolonged residence time, likely resulted in partial gas loss from the system and increased occurrences of cell collapse and coalescence.

Examining the SEM images of samples printed at higher temperatures but at increased speeds revealed a notable difference in structure. The irregular morphology observed at low speeds disappeared, and instead, the cellular structure exhibited well-defined, circular pores with higher cell density, forming a more homogeneous foam morphology. This indicates that at elevated speeds, the reduced residence time minimized excessive heat exposure, preserving the polymer's melt strength while simultaneously benefiting from the increased pressure drop, which enhanced cell nucleation.

Table 1. SEM images of the structures printed with different temperature and speed settings.

Printing speed [mm/s]	220 °C printing temperature	230 °C printing temperature	240 °C printing temperature	250 °C printing temperature
20				
30				
40				
50				
60				

The structural trends observed in the SEM images are further supported by quantitative image analysis of the cellular structure (see Figure 5). Cell density, defined as the number of cells per unit volume, increased with printing speed across all conditions except for the lower temperature (220 and 230 °C) prints. At 220 °C, foaming was limited due to insufficient gas evolution. At 230 °C, no clear trend was observed, as higher printing speeds reduced the amount of gas released during the initial stage of foaming due to shortened residence time (Figure 3), while simultaneously enhancing cell nucleation through increased pressure drop [36]. At higher

temperatures, the correlation between printing speed and cell density became more apparent, supporting the previously discussed role of pressure drop at the nozzle exit in promoting the formation of nucleation sites.

Cell size generally increased with printing temperature, indicating that higher temperatures allowed for a more extensive expansion phase before the structure was solidified by cooling. However, increasing printing speed led to a slight reduction in average cell size. This trend can be attributed to two factors: (1) reduced expansion time before solidification at higher speeds and (2) the increased number of

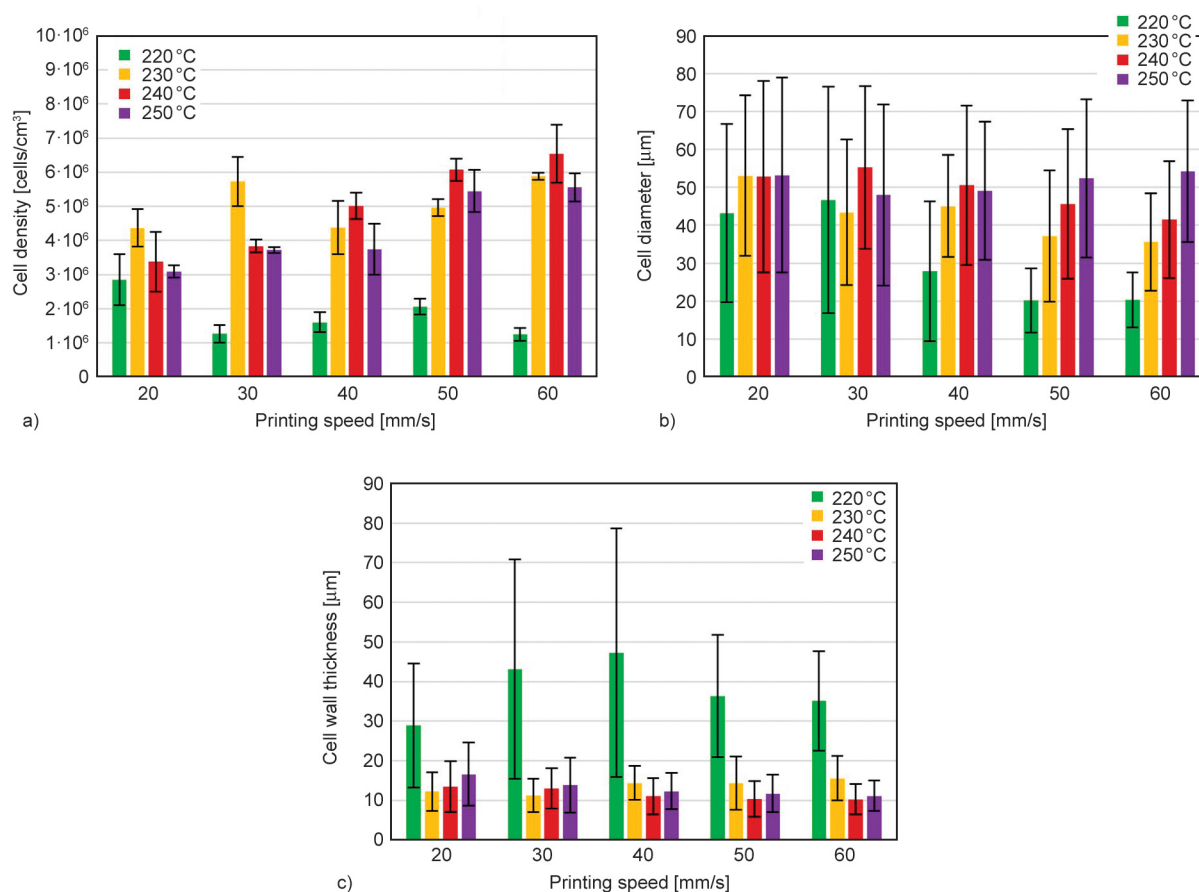


Figure 5. Cell density (a), cell diameter (b) and cell wall thickness (c) characteristics of the foam structures printed with different temperature and speed settings.

nucleated cells, which resulted in a finer cellular structure due to a more distributed gas phase.

Finally, cell wall thickness remained relatively constant across the samples where significant foaming occurred. This suggests that while printing parameters influenced the number and size of cells, they did not cause significant variations in their cell wall dimensions.

3.2. Effect of nozzle diameter on foam structure and density

To investigate the influence of nozzle diameter on the foaming process, specimens were printed using 0.4, 0.6, and 0.8 mm nozzles at constant printing speed while varying the temperature between 220 and 250 °C. The SEM images of the printed samples are summarized in Table 2, illustrating the effect of nozzle diameter on foaming.

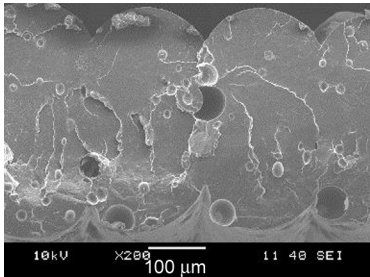
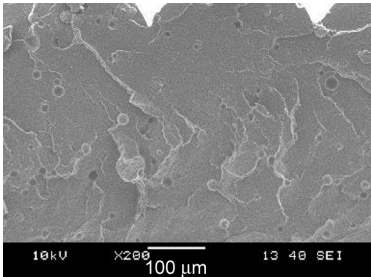
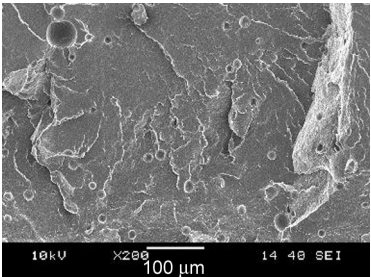
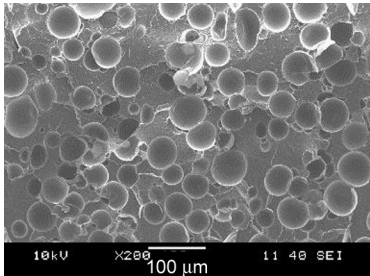
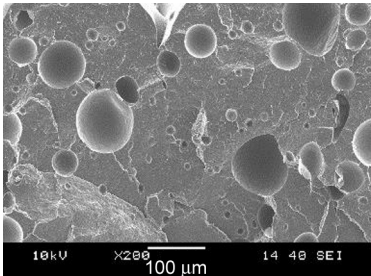
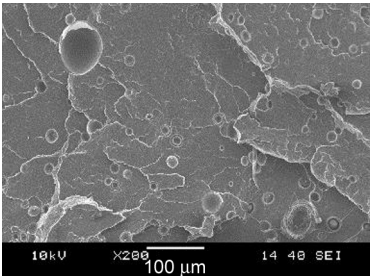
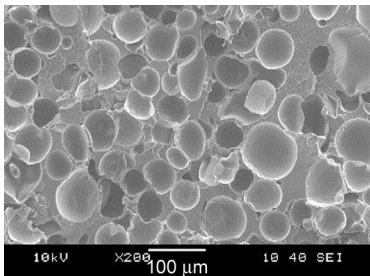
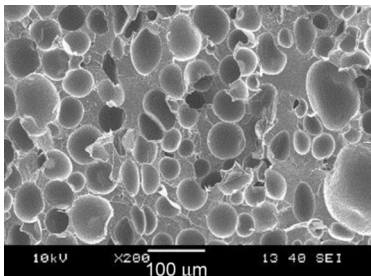
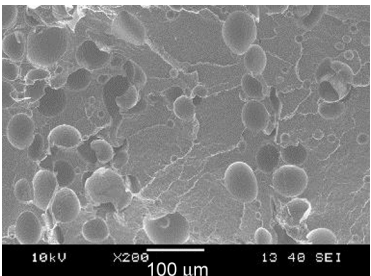
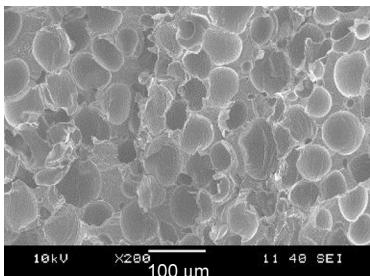
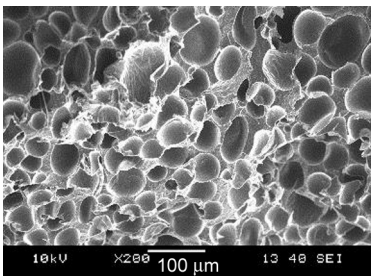
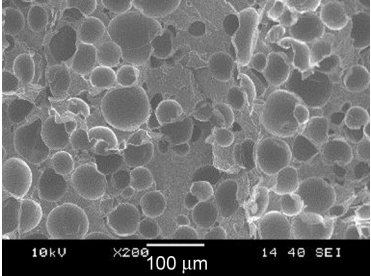
The results indicate that, in terms of maximizing foaming efficiency, smaller nozzle diameters are preferable. Despite many filament manufacturers recommending the use of larger nozzles for *in-situ* foaming PLA due to the pre-expanded nature of

these materials, our findings suggest that a smaller nozzle leads to greater expansion and porosity.

This phenomenon can likely be attributed to two key factors. First, with a reduced cross-sectional area, the filament requires less time to reach the target temperature across its cross-section. At the same time, smaller nozzle diameters result in longer residence times (see Figure 3), allowing the blowing agent more time to decompose and the gas to dissolve into the polymer matrix more effectively. Second, a smaller nozzle subjects the material to greater shear forces, which enhances internal friction and heat generation due to viscous heating [37]. Additionally, the increased shear may contribute to a higher pressure inside the nozzle, resulting in a more significant pressure drop upon exit from the nozzle [35], which promotes cell nucleation [36].

The density measurement results (Figure 6) also confirm this trend, showing that at each tested temperature, the lowest density – and consequently, the highest expansion – was achieved with the smallest nozzle. An exception to this tendency was observed at 220 °C, where the density values remained high

Table 2. SEM images of the structures printed at different temperatures using different nozzle diameters.

Printing temperature [C°]	Nozzle diameter [mm]		
	0.4	0.6	0.8
220			
230			
240			
250			

regardless of the nozzle diameter, indicating that the temperature was insufficient to initiate effective foaming. This observation is supported by the SEM images shown Table 2, where only a minimal number of pores – or in some cases, none – can be observed. Although the 0.4 mm nozzle provided higher shear rates, the total thermal input – resulting from the combination of residence time and viscous heating – was still inadequate to trigger the decomposition of the blowing agent and initiate cell nucleation at this low temperature.

The cell structural characteristics extracted from SEM images (Figure 7) reveal that above 230 °C, smaller nozzle diameters led to an increased number of nucleated cells per unit volume, resulting in higher cell density. This is a direct consequence of the greater pressure drop, which promotes bubble nucleation. Furthermore, while cell diameter remained relatively stable across different nozzle sizes, a slight increase was observed for smaller nozzles. This is presumably related to the longer residence time (see Figure 3), which may have led to more gas formation, and to the

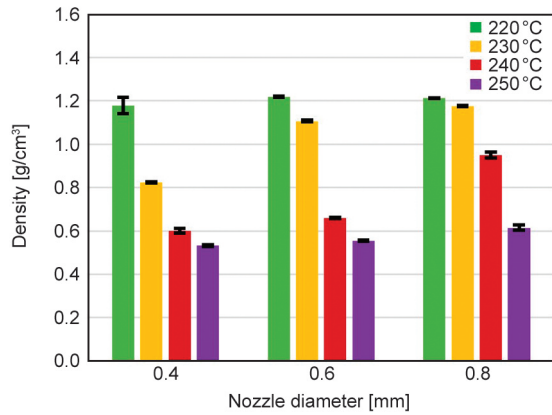


Figure 6. Density results of the structures printed at different temperatures using different nozzle sizes.

fact that the material likely reached the target temperature more uniformly across the cross-section, allowing for a longer cell growth period before the polymer solidifies and stabilizes the foam structure.

While these effects were still observable at 250 °C, the influence of nozzle diameter on density and structure became less distinct compared to lower temperatures (Figure 6). As shown in Figure 7, cell density was still higher for smaller nozzle diameters,

suggesting enhanced nucleation. The average cell size remained relatively stable, but SEM images (Table 2) indicate that samples printed with larger nozzles exhibited a more heterogeneous cell distribution, including a few larger pores, regions lacking visible cells, and areas with only partially expanded structures. These structural irregularities balanced each other out, resulting in similar average cell sizes despite the visible differences in foam morphology. At this elevated temperature, the reduced pressure drop associated with larger nozzle diameters may shift the balance between nucleation and growth, resulting in fewer nucleated cells. These cells, however, can grow larger as more gas diffuses into them [38, 39]. The lower internal pressure in these expanding bubbles facilitates additional gas uptake, amplifying cell growth over nucleation and forming larger, more isolated pores.

These findings highlight that selecting an appropriate nozzle diameter is a crucial parameter for optimizing *in-situ* foaming efficiency, as it directly influences the extent of expansion, cell nucleation, and final cellular morphology.

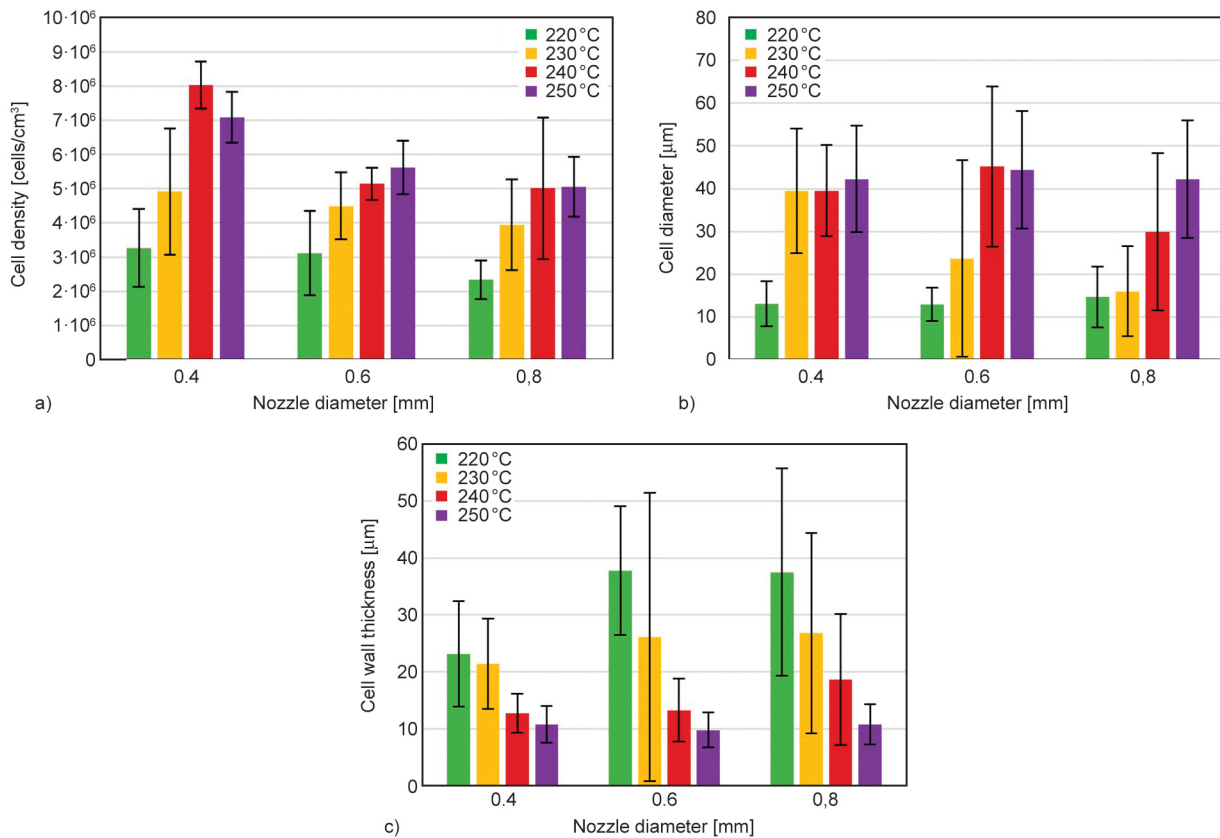


Figure 7. Cell density (a), cell diameter (b) and cell wall thickness (c) characteristics of the foam structures printed at different temperatures using different nozzle sizes.

3.3. Functionally graded foams: Effect of temperature-controlled layering on mechanical properties

3.3.1. 3D-printing

According to the method described in Section 2.2.4., we created 4-layer graded structures, in which the porosity of each layer were controlled by modifying the printing temperature and compensating the change in volume due to foaming with the extrusion multiplier. The SEM images taken from the cryogenic fracture surfaces of each configuration are presented in Figure 8.

As shown in Figure 8, some minor voids can be observed between the layers, especially in the non-foamed regions. These are likely due to the lack of expansion, which generally helps to fill small gaps between layers. It is important to note that increasing the flow rate could help eliminate these interfacial

voids, as more material would be deposited in each layer. In this study, however, we adjusted the extrusion parameters only to maintain the same overall dimensions and mass for each configuration, so that the effect of layer arrangement could be compared directly.

3.3.2. Three-point bending

The results of the three-point bending tests are summarized in Figure 9, illustrating the force-deformation curves, the flexural strength and modulus for each graded structure. The results clearly show the influence of the layer configuration on the mechanical performance, demonstrating that the control over porosity by adjusting the printing parameters can significantly enhance flexural resistance.

The 210–250–250–210 configuration, which has dense outer layers and a porous core, exhibited the

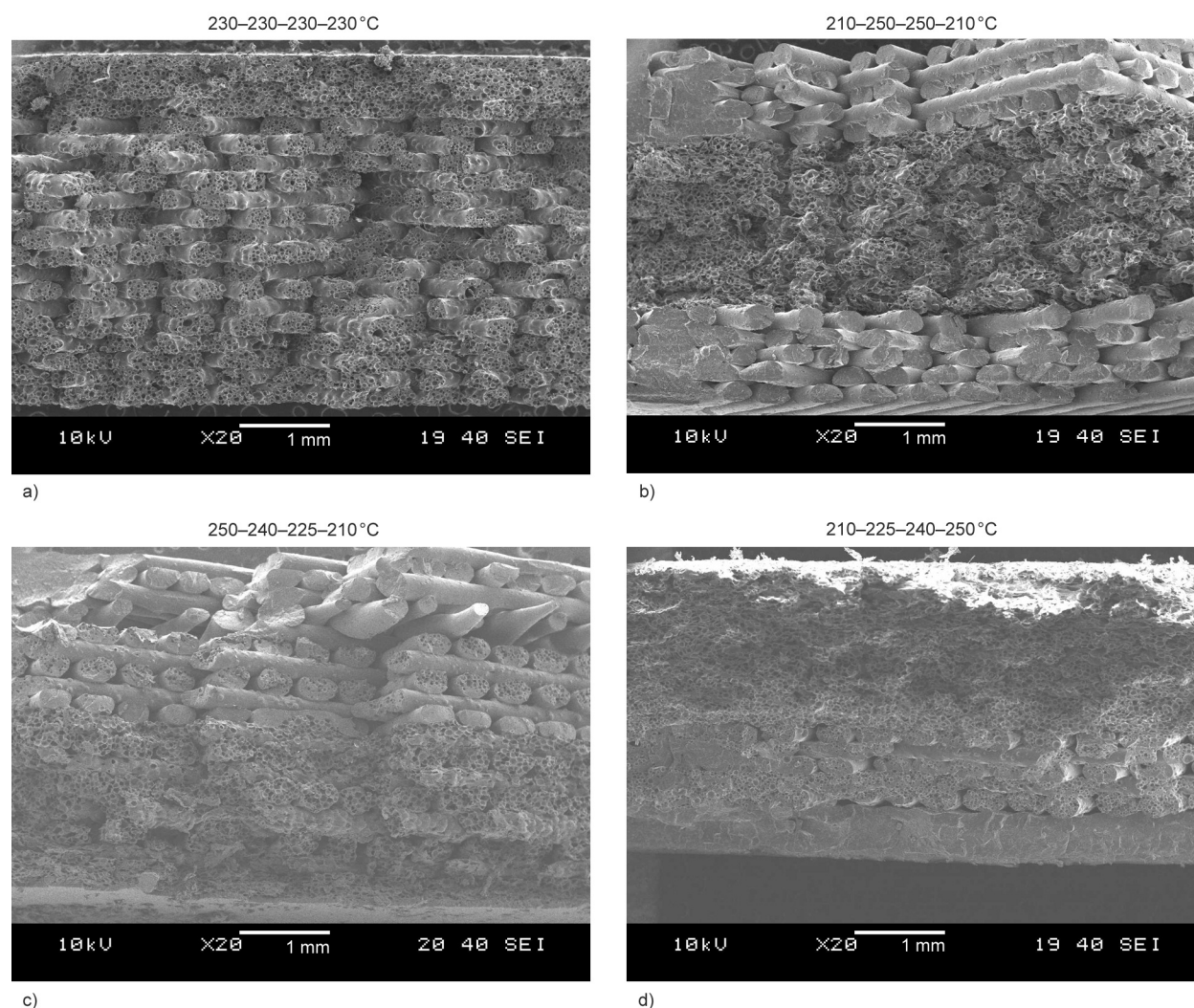


Figure 8. SEM images of the four-layer graded structures printed with different temperatures applied to each layer. a) printed with 230–230–230–230 °C, b) with 210–250–250–210 °C, c) with 250–240–225–210 °C and d) with 210–225–240–250 °C.

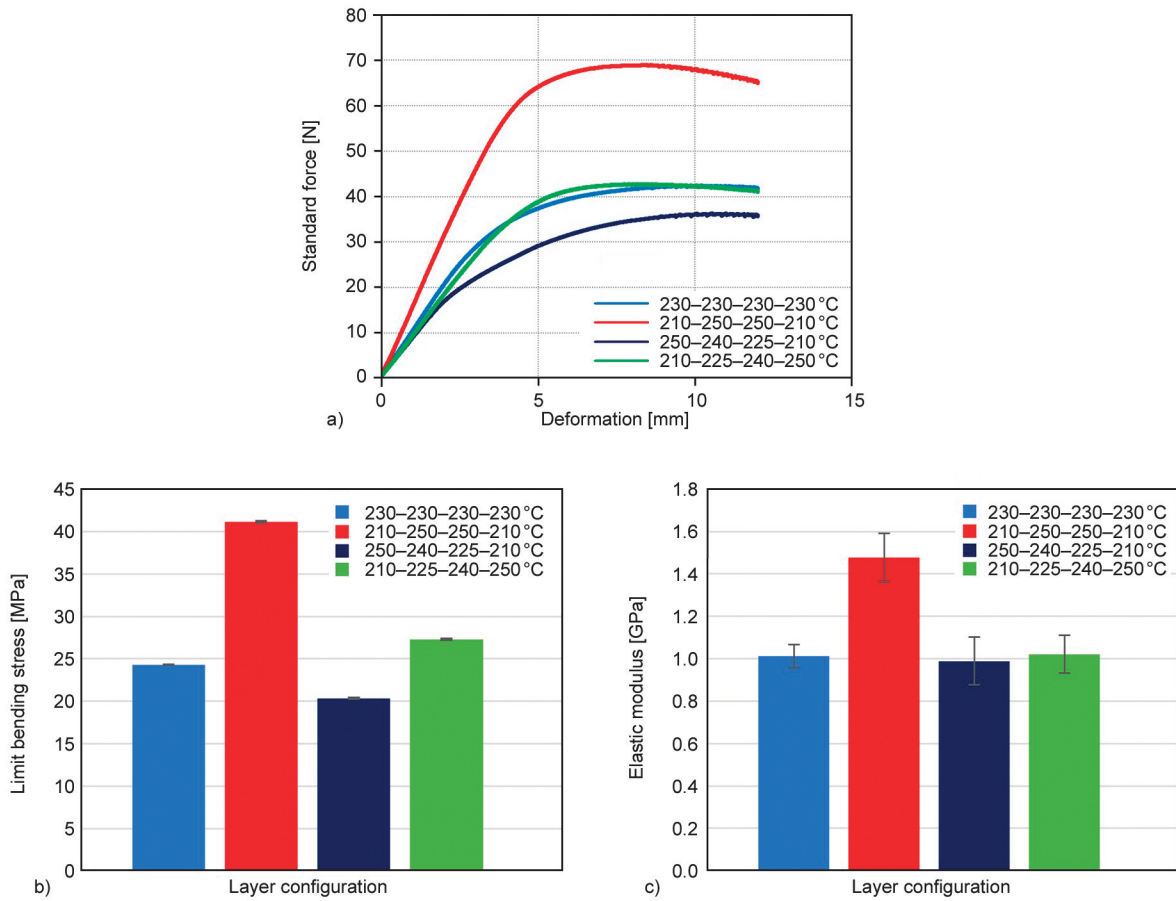


Figure 9. Force-deformation curves (a), limit bending stress (b) and elastic modulus (c) results obtained from the 3-point bending test.

highest flexural strength (41.15 ± 1.955 MPa) and modulus among all tested structures. This outcome can be explained by the general stress distribution in bending, where the top and bottom layers experience the highest compressive and tensile stresses, respectively. Since these layers had the highest density, they provided enhanced resistance to deformation, while the porous core reduced weight without significantly compromising stiffness. This design maximized mechanical performance while minimizing mass, demonstrating the efficiency of a shell-core-shell design for bending loads. The deformation remained largely elastic up to relatively high loads, with visible deflection but no sudden failure, indicating stable load-bearing behavior of the dense outer layers.

In contrast, the homogeneous structure (230–230–230–230) exhibited a significantly lower flexural strength (24.3 ± 1.022 MPa). In this case, the stress was evenly distributed throughout the sample, preventing localized strengthening in the most highly stressed regions. This confirms that material grading plays a

crucial role in optimizing bending performance by reinforcing the areas subjected to the highest loads. For graded structures with progressively changing density, the flexural strength varied depending on the direction of the density gradient. The 210–225–240–250 configuration, where the upper layers were more porous and the lower layers denser, exhibited higher strength (27.296 ± 0.836 MPa) than its inverse counterpart (250–240–225–210, 20.351 ± 1.193 MPa). This trend is closely related to the general mechanical behavior of cellular materials, as foams tend to be more resistant to compressive loads than tensile loads. In bending, the top layer undergoes compression, while the bottom layer is subjected to tensile stress. In the 210–225–240–250 structure, the densest layer was positioned at the bottom, reinforcing the region most sensitive to tensile loads, while the upper porous layer was able to deform progressively and withstand stress under compression. In contrast, in the 250–240–225–210 structure, the bottom layer was more porous, reducing its ability to withstand tensile loads, which led to lower flexural strength.

3.3.3. Impact testing

The results of the impact tests are presented in Figure 10, which shows the peak force, perforation energy, and ductility index for each tested layer configuration.

The data indicate that modifying the layer order consistently increased the force required to initiate crack propagation and the energy needed for complete perforation compared to the homogeneous structure (printed at 230 °C). However, the ductility index decreased, suggesting that functionally graded structures exhibited a more brittle failure than the homogeneous reference specimen. To better understand these differences, we analyzed the force-time curves (see Figure 11) recorded during the tests.

The impact response of the different layer configurations varied significantly, as reflected in their force-time curves and derived mechanical parameters. The homogeneous structure (230–230–230–230) exhibited the lowest peak force (461.9 ± 53.9 N) and the highest ductility index ($80.6 \pm 11.4\%$). The force reached its maximum within 1 ms and then gradually

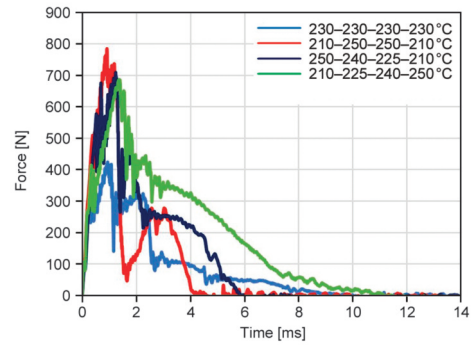


Figure 11. Typical force-time curves recorded during the impact tests.

declined over 8 ms, indicating a relatively extended failure duration. This suggests a failure mechanism, where energy dissipation occurs gradually throughout the structure. However, despite its ability to undergo gradual deformation, this configuration had the lowest perforation energy (0.89 ± 0.17 J/mm), highlighting its limited capacity to resist impact due to the lack of energy-dissipating effects provided by the graded structures. The failure occurred through gradual crack initiation and propagation through the

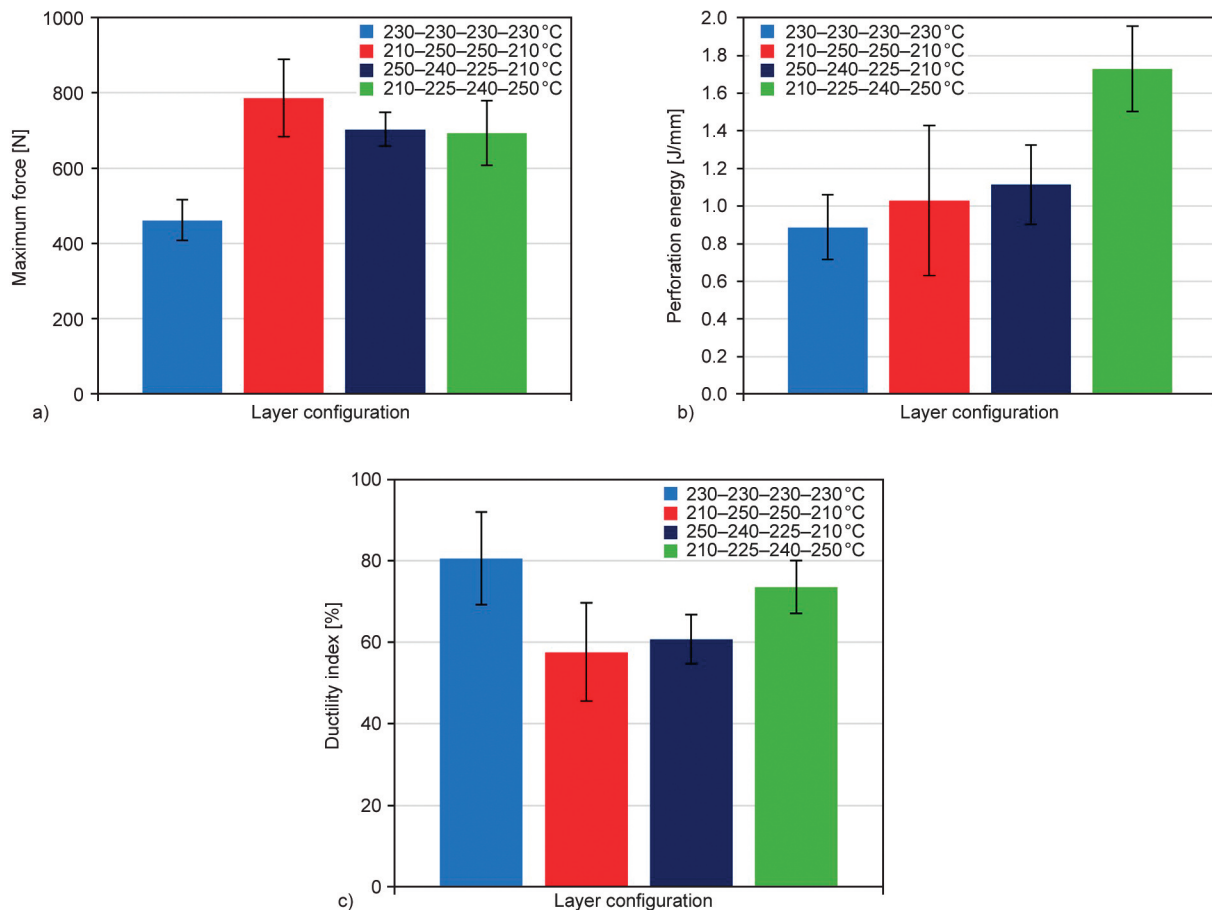


Figure 10. Impact testing results of the density-graded printed samples: maximum force (a), perforation energy (b), and ductility index (c).

thickness, with less pronounced brittle fracture surfaces observed compared to graded structures.

In contrast, the configuration with denser outer layers and a porous core (210–250–250–210) exhibited the highest peak force (785.6 ± 103.1 N), which was reached within 1.1 ms. However, this was followed by the most rapid failure progression, with complete perforation occurring in just 4 ms. The force-time curve demonstrated a steep increase in force, followed by a rapid drop, suggesting that the stiff outer layers initially provided significant resistance, but the weak, porous core collapsed quickly, leading to brittle failure. The low ductility index ($57.6 \pm 12.0\%$) further confirms that while this configuration effectively resisted the initial impact, it facilitated early structural failure due to insufficient energy dissipation.

A different trend was observed in the configuration where porosity increased toward the top (210–225–240–250). This structure exhibited the highest perforation energy (1.73 ± 0.23 J/mm), indicating superior energy absorption capacity. The force-time curve revealed a delayed force drop, with the peak force (692.3 ± 86.2 N) occurring at 1.5 ms, followed by a gradual decline over 11 ms before complete perforation. The extended failure duration suggests that energy was dissipated progressively through the increasingly stiff lower layers, which delayed crack propagation and structural collapse. The fracture surface showed progressive damage development, with visible crushing and compaction of the porous top layers prior to final rupture.

The configuration with decreasing porosity toward the top (250–240–225–210) exhibited a similar peak force (703.3 ± 44.5 N) to its counterpart with increasing porosity, yet its perforation energy (1.11 ± 0.21 J/mm) was notably lower. The force-time curve showed a sharp initial force increase followed by a relatively rapid drop, with complete perforation occurring within 6 ms. This behavior suggests a more sudden failure, likely due to the inability of the porous bottom layer to provide sufficient resistance and slow down crack propagation. These trends are in good agreement with the literature, which highlights that the density of the top layer – being the first to contact the impactor – has a dominant influence on the initial slope of the force-time curve. A decreasing density gradient in the loading direction results in weaker lower sections, offering less resistance and allowing deformation to progress more

rapidly toward the end of the impact event [19]. The lower ductility index ($57.6 \pm 12.0\%$) further supports this observation, indicating that while peak resistance remained similar, the overall energy absorption capacity of this configuration was decreased.

These results clearly demonstrate that the layer order and orientation have a significant influence on the impact behavior of the printed structures. By properly adjusting the density gradient, it is possible to optimize the strength–weight balance for a given application. In addition to the orientation, the exact shape of the density profile (e.g., linear, concave, convex) may also affect the mechanical performance, as suggested by previous studies [19, 40, 41], and could be the subject of future investigations.

4. Conclusions

In this study, we systematically investigated the influence of processing parameters on the foaming behavior and cellular structure of *in-situ* foam 3D-printed specimens. By analyzing the combined effects of printing temperature and speed, we identified their roles in the four key stages of the foaming process: gas dissolution, cell nucleation, cell growth, and stabilization. Our results demonstrated that increasing the printing temperature generally enhances foaming by promoting greater gas evolution and expansion. However, excessive heat exposure at low printing speeds led to irregular cell structures due to premature cell collapse and coalescence. Conversely, higher printing speeds improved cell nucleation efficiency by increasing the pressure drop at the nozzle exit, but at the same time, excessively high speeds limited foaming due to the reduced residence time, which was insufficient for complete gas dissolution in the polymer matrix.

We also explored the effect of nozzle diameter, an aspect previously unexamined in the context of *in-situ* foam 3D printing. Our findings revealed that smaller nozzle diameters enhance foaming efficiency by improving heat transfer, increasing shear-induced nucleation, and promoting higher internal pressures, which lead to a greater pressure drop when the melted polymer exits the nozzle.

To further demonstrate process-controlled foaming, we fabricated functionally graded four-layer structures by varying the printing temperature per layer. Mechanical tests showed that layer order significantly influences the bending and impact resistance of the graded structures. Specimens with dense outer

layers and a porous core exhibited superior bending strength. At the same time, structures with an increasing porosity gradient from bottom to top provided the best balance between strength and energy absorption under impact loading. These results highlight the potential of *in-situ* foam 3D printing for producing lightweight cellular materials with tailored mechanical properties.

Our findings contribute to a deeper understanding of process-controlled foaming in additive manufacturing and provide valuable insights for optimizing *in-situ* foam 3D printing for structural applications. Future research may focus on refining nozzle geometries, developing custom filament formulations – including foaming filaments made from recycled polymers – and exploring advanced strategies to enhance foaming efficiency. In addition, the influence of flow rate and extrusion volume on the foaming process should also be investigated, as these parameters may significantly affect layer adhesion. These results have potential applications in medical technology, particularly in the development of orthotic devices and implants, as well as in energy-absorbing systems for the automotive and sports equipment industries. Additionally, they contribute to improving the functionality of FDM-printed parts, thereby supporting the broader adoption of this technology in various engineering fields.

Acknowledgements

Project no. TKP-6-6/PALY-2021 has been implemented with the support provided by the Ministry of Culture and Innovation of Hungary from the National Research, Development and Innovation Fund, financed under the TKP2021-NVA funding scheme. This research was supported by the National Research, Development and Innovation Office, Hungary (K 146236). Project no KDP-IKT-2023-900-I1-00000957/0000003 has been implemented with the support provided by the Ministry of Culture and Innovation of Hungary from the National Research, Development and Innovation Fund, financed under the KDP-2023 funding scheme.

References

- [1] Shanthar R., Chen K., Abeykoon C.: Powder-based additive manufacturing: A critical review of materials, methods, opportunities, and challenges. *Advanced Engineering Materials*, **25**, 2300375 (2023).
<https://doi.org/10.1002/adem.202300375>
- [2] Shahrubudin N., Lee T. C., Ramlan R.: An overview on 3D printing technology: Technological, materials, and applications. *Procedia Manufacturing*, **35**, 1286–1296 (2019).
<https://doi.org/10.1016/j.promfg.2019.06.089>
- [3] Avcioglu E.: Surface texture effects on mechanical properties of additively manufactured polylactic acid. *Express Polymer Letters*, **19**, 3–14 (2025).
<https://doi.org/10.3144/expresspolymlett.2025.2>
- [4] da Silva Siqueira A., Braga N. F., Muñoz P. A. R. de Freitas L. F., Ferreira A. H., Fachine G. J. M.: Biodegradable scaffold: Integration of polylactic acid, hydroxyapatite, and graphene oxide via FDM 3D printing. *Express Polymer Letters*, **18**, 656–672 (2024).
<https://doi.org/10.3144/expresspolymlett.2024.48>
- [5] Kónya G., Ficzer P.: The effect of layer thickness and orientation of the workpiece on the micro- and macrogeometric properties and the machining time of the part during 3D printing. *Periodica Polytechnica Mechanical Engineering*, **67**, 143–150 (2023).
<https://doi.org/10.3311/PPme.21473>
- [6] Alduais A., Özerinç S.: Tunable mechanical properties of thermoplastic foams produced by additive manufacturing. *Express Polymer Letters*, **17**, 317–333 (2023).
<https://doi.org/10.3144/expresspolymlett.2023.23>
- [7] Jain P. K., Jain P. K.: Use of 3D printing for home applications: A new generation concept. *Materials Today: Proceedings*, **43**, 605–607 (2021).
<https://doi.org/10.1016/j.matpr.2020.12.145>
- [8] Pan A. Q., Huang Z. F., Guo R. J., Liu J.: Effect of FDM process on adhesive strength of polylactic acid (PLA) filament. *Key Engineering Materials*, **667**, 181–186 (2016).
<https://doi.org/10.4028/www.scientific.net/KEM.667.181>
- [9] Kalia K., Francoeur B., Amirkhizi A., Ameli A.: *In situ* foam 3D printing of microcellular structures using material extrusion additive manufacturing. *ACS Applied Materials and Interfaces*, **14**, 22454–22465 (2022).
<https://doi.org/10.1021/acsami.2c03014>
- [10] Nofar M., Utz J., Geis N., Altstädt V., Ruckdäschel H.: Foam 3D printing of thermoplastics: A symbiosis of additive manufacturing and foaming technology. *Advanced Science*, **9**, 2105701 (2022).
<https://doi.org/10.1002/advs.202105701>
- [11] Li M., Jiang J., Hu B., Zhai W.: Fused deposition modeling of hierarchical porous polyetherimide assisted by an *in-situ* CO₂ foaming technology. *Composites Science and Technology*, **200**, 108454 (2020).
<https://doi.org/10.1016/j.compscitech.2020.108454>
- [12] Sun B., Wu L.: Research progress of 3D printing combined with thermoplastic foaming. *Frontiers in Materials*, **9**, 1083931 (2022).
<https://doi.org/10.3389/fmats.2022.1083931>

- [13] Zhang S., Shi X., Miao Z., Zhang H., Zhao X., Wang K., Qin J., Zhang G.: 3D-printed polyurethane tissue-engineering scaffold with hierarchical microcellular foam structure and antibacterial properties. *Advanced Engineering Materials*, **24**, 2101134 (2022).
<https://doi.org/10.1002/adem.202101134>
- [14] Kalia K., Kazmer D., Ameli A.: A co-extrusion additive manufacturing process with mixer nozzle to dynamically control blowing agent content and print functionally graded foams. *ACS Applied Engineering Materials*, **3**, 625–635 (2025).
<https://doi.org/10.1021/acsaenm.4c00764>
- [15] Tomin M., Kmetty Á.: Polymer foams as advanced energy absorbing materials for sports applications – A review. *Journal of Applied Polymer Science*, **139**, e51714 (2022).
<https://doi.org/10.1002/app.51714>
- [16] Tomin M., Török D., Pászthy T., Kmetty Á.: Deformation analysis in impact testing of functionally graded foams by the image processing of high-speed camera recordings. *Polymer Testing*, **122**, 108014 (2023).
<https://doi.org/10.1016/j.polymertesting.2023.108014>
- [17] Kalia K., Amirkhizi A., Ameli A.: The effect of melt flow rate and print speed on the density and microcellular structure of 3D printed polylactic acid foams. *AIP Conference Proceedings*, **2884**, 140003 (2023).
<https://doi.org/10.1063/5.0168370>
- [18] Kalia K., Ameli A.: Understanding the process-microstructure-property relationships in material extrusion additive manufacturing of polylactic acid microcellular foams. *Additive Manufacturing*, **72**, 103636 (2023).
<https://doi.org/10.1016/j.addma.2023.103636>
- [19] Kalia K., Ameli A.: Additive manufacturing of functionally graded foams: Material extrusion process design, part design, and mechanical testing. *Additive Manufacturing*, **79**, 103945 (2024).
<https://doi.org/10.1016/j.addma.2023.103945>
- [20] Nieduzak Z., Hart S., Joseph Y., Kalia K., Ameli A.: *In-situ* foam 3D-printing of recycled HDPE/PP blend. in ‘SPE FOAMS 2022. Indianapolis, USA’, 1–5 (2022).
- [21] Peng K., Chen S., Senthoooran V., Hu X., Qi Y., Zhang C., Wu L., Wang J.: Microporous polylactic acid/chitin nanocrystals composite scaffolds using *in-situ* foaming 3D printing for bone tissue engineering. *International Journal of Biological Macromolecules*, **279**, 135055 (2024).
<https://doi.org/10.1016/j.ijbiomac.2024.135055>
- [22] Zhang S., Gao Q., Zhang Y., Sheng X., Miao Z., Qin J., Zhang G., Shi X.: 3D printing thermoplastic polyurethane hierarchical cellular foam with outstanding energy absorption capability. *Additive Manufacturing*, **76**, 103770 (2023).
<https://doi.org/10.1016/j.addma.2023.103770>
- [23] Damanpack A. R., Sousa A., Bodaghi M.: Porous PLAs with controllable density by FDM 3D printing and chemical foaming agent. *Micromachines*, **12**, 866 (2021).
<https://doi.org/10.3390/mi12080866>
- [24] Ozdemir M., Doubrovski Z.: Xpandables: Single-filament multi-property 3D printing by programmable foaming. in ‘Extended Abstracts of the 2023 CHI Conference on Human Factors in Computing Systems. Hamburg, Germany’, 1–7 (2023).
- [25] Choi W. J., Hwang K. S., Kwon H. J., Lee C., Kim C. H., Kim T. H., Heo S. W., Kim J-H., Lee J-Y.: Rapid development of dual porous poly(lactic acid) foam using fused deposition modeling (FDM) 3D printing for medical scaffold application. *Materials Science and Engineering: C*, **110**, 110693 (2020).
<https://doi.org/10.1016/j.msec.2020.110693>
- [26] Son Y.: Determination of shear viscosity and shear rate from pressure drop and flow rate relationship in a rectangular channel. *Polymer*, **48**, 632–637 (2007).
<https://doi.org/10.1016/j.polymer.2006.11.048>
- [27] Kanani A. Y., Kennedy A.: Effect of the material extrusion process parameters on the compressive properties of additively manufactured foamed and nonfoamed polylactic acid structures. *3D Printing and Additive Manufacturing*, **11**, 207-218 (2024).
<https://doi.org/10.1089/3Dp.2022.0091>
- [28] Tomin M., Lukács N., Berezvai S.: Development of density-graded sandwich structures with *in-situ* foaming filaments in additive manufacturing. in ‘Proceedings of the FOAMS 2024 Conference. King of Prussia, USA’ 1–7 (2024).
- [29] Kmetty Á., Litauszki K.: Development of poly(lactide acid) foams with thermally expandable microspheres. *Polymers*, **12**, 463 (2020).
<https://doi.org/10.3390/polym12020463>
- [30] Gosselin R., Rodrigue D.: Cell morphology analysis of high density polymer foams. *Polymer Testing*, **24**, 1027–1035 (2005).
<https://doi.org/10.1016/j.polymertesting.2005.07.005>
- [31] Tomin M., Kmetty Á.: Evaluating the cell structure-impact damping relation of cross-linked polyethylene foams by falling weight impact tests. *Journal of Applied Polymer Science*, **138**, 49999 (2021).
<https://doi.org/10.1002/app.49999>
- [32] Rangappa R., Yeh S-K.: Investigating the role and impact of N₂ as a blowing agent in the fabrication of thermoplastic polyurethane foams. *Cellular Polymers*, **42**, 187–203 (2023).
<https://doi.org/10.1177/02624893231203376>
- [33] ASTM D790-17: Standard test methods for flexural properties of unreinforced and reinforced plastics and electrical insulating materials (2017).
- [34] Tomin M., Kmetty Á.: Investigation of the energy absorption properties of cross-linked polyethylene foams. *IOP Conference Series: Materials Science and Engineering*, **903**, 012059 (2020).
<https://doi.org/10.1088/1757-899X/903/1/012059>

- [35] de Vries S., Schuller T., Galindo-Rosales F. J., Fanzio P.: Pressure drop non-linearities in material extrusion additive manufacturing: A novel approach for pressure monitoring and numerical modeling. *Additive Manufacturing*, **80**, 103966 (2024).
<https://doi.org/10.1016/j.addma.2024.103966>
- [36] Park C. B., Baldwin D. F., Suh N. P.: Effect of the pressure drop rate on cell nucleation in continuous processing of microcellular polymers. *Polymer Engineering and Science*, **35**, 432–440 (1995).
<https://doi.org/10.1002/pen.760350509>
- [37] Rosenbaum E. E., Hatzikiriakos S. G.: Wall slip in the capillary flow of molten polymers subject to viscous heating. *AIChE Journal*, **43**, 598–608 (1997).
<https://doi.org/10.1002/aic.690430305>
- [38] Alavi S., Rizvi S. S. H.: Strategies for enhancing expansion in starch-based microcellular foams produced by supercritical fluid extrusion. *International Journal of Food Properties*, **8**, 23–34 (2005).
<https://doi.org/10.1081/JFP-200048139>
- [39] Gandhi A., Bhatnagar N.: Die opening-induced microstructure growth in extrusion foaming of thermoplastic sheets. *Journal of Polymer Engineering*, **36**, 129–138 (2016).
<https://doi.org/10.1515/polyeng-2015-0234>
- [40] Koohbor B., Kidane A.: Design optimization of continuously and discretely graded foam materials for efficient energy absorption. *Materials and Design*, **102**, 151–161 (2016).
<https://doi.org/10.1016/j.matdes.2016.04.031>
- [41] Cui L., Kiernan S., Gilchrist M. D.: Designing the energy absorption capacity of functionally graded foam materials. *Materials Science and Engineering: A*, **507**, 215–225 (2009).
<https://doi.org/10.1016/j.msea.2008.12.011>